

Compressed Multiband Sensing in FR3 Using Alternating Direction Method of Multipliers

Dexin Wang^{*†}, Isha Jariwala[†], Ahmad Bazzi^{*†}, Sundeep Rangan[†], Theodore S. Rappaport[†], and Marwa Chafii^{*†}

^{*}Engineering Division, New York University (NYU) Abu Dhabi, Abu Dhabi, UAE.

[†]NYU WIRELESS, NYU Tandon School of Engineering, New York, USA

Abstract—Joint detection and localization of users and scatterers in multipath-rich channels on multiple bands is critical for integrated sensing and communication (ISAC) in 6G. Existing multiband sensing methods are limited by classical beamforming or computationally expensive approaches. This paper introduces alternating direction method of multipliers (ADMM)-assisted compressed multiband sensing (CMS), hereafter referred to as ADMM-CMS, which is a novel framework for multiband sensing using uplink QAM-modulated pilot symbols. To solve the CMS problem, we develop an adaptive ADMM algorithm that adjusts to noise and ensures automatic stopping if converged. ADMM combines the decomposability of dual ascent with the robustness of augmented Lagrangian methods, making it suitable for large-scale structured optimization. Simulations show that ADMM-CMS achieves higher spatial resolution and improved denoising compared to Bartlett-type beamforming, yielding a 34 dB gain in per-antenna transmit power for achieving a 0.9 successful recovery probability (SRP). Moreover, compared to performing compressed sensing separately on the constituent 7 GHz and 10 GHz sub-bands, ADMM-CMS achieves reductions in delay root mean squared error of 35% and 38.1%, respectively, at -41 dBm per-antenna transmit power, while also yielding improved SRP. Our findings demonstrate ADMM-CMS as an efficient enabler of ISAC in frequency range 3 (FR3, 7-24 GHz) for 6G systems.

Index Terms—compressed sensing, multiband sensing, joint angle-delay estimation, localization, ISAC, FR3, 6G, ADMM

I. INTRODUCTION

The integration of wireless communications and radar sensing, known as integrated sensing and communication (ISAC), has recently been proposed as one of the six usage scenarios in IMT-2030 (6G), and has become a practical necessity for 6G wireless systems [1]. To save resources in spectrum, processing power, and hardware, which were traditionally allocated separately for sensing and communications, ISAC systems must not only deliver multi-gigabit data rates but also jointly detect and localize people, vehicles, and objects in the environment with high accuracy [2]. Thus, ISAC systems are envisioned to efficiently foster future applications of 6G networks such as internet of things, smart cities, and autonomous driving. In communication-centric ISAC, the goal is to perform sensing via existing communication symbols such as pilots. Compressed sensing (CS) provides an elegant solution to ISAC problems, offering reduced noise [3], hence suppression of false target detection. From a communication-centric ISAC perspective, in order to maintain sensing performance, CS requires less sacrifice in communication resources such as the orthogonal frequency-division multiplexing (OFDM) resource elements (REs) as CS enables sub-Nyquist sampling.

The introduction of new frequency bands for cellular mobile communication, such as frequency range 3 (FR3, 7–24 GHz), prompted multiband sensing to become an enabler of ISAC, allowing the ability to take advantage of both the coverage of the lower bands and the spatial resolution of the higher bands (due to narrower beams) to improve the sensing accuracy and even help reduce ambiguities, such as grating lobes [4]–[6]. This combination of different bands is enabled by the important property that the angles and delays of the targets remain relatively constant across sub-bands while their amplitudes may vary [5], [7]. Throughout this paper, we assume sub-band bandwidths in the hundreds of MHz range, consistent with FR3 allocations [8]. Within upper mid-band, angular spread and delay spread remain relatively constant, with only minor frequency dependence. Moreover, fragmented spectrum allocations and frequency-dependent channel behavior [8], [9] in FR3 make multiband sensing more suitable.

Past work on joint detection and localization has relied heavily on classical beamforming (BF). Bartlett and Capon beamformers have been widely studied for localization, but their resolution is limited by array aperture, and they suffer under low-SNR conditions [10]. Iterative refinements on the estimated parameters such as the space alternating generalized expectation-maximization (SAGE) algorithm [11], [12] improve estimation accuracy but at the expense of complexity. The liquid neural network-enabled BF might provide a potential solution for accurate localization [13]. Approaches not relying on peak-finding on a discrete angle-delay grid such as atomic norm minimization or subspace methods achieve excellent resolution but remain computationally expensive and difficult to scale in multiband scenarios [14]. Although recent studies in FR3 have begun to explore multiband localization [8], [10], most existing approaches continue to rely on BF-based estimators instead of sparse recovery methods such as CS [15]. In this paper, our contributions are as follows:

- We propose alternating direction method of multipliers (ADMM)-assisted compressed multiband sensing (CMS), hereafter referred to as ADMM-CMS, which is a new framework of using CS to perform multiband ISAC on FR3 using QAM-modulated communication pilot symbols in the uplink. We formulate the multiband joint angle-delay estimation problem as a structured sparse recovery task.
- We develop an ADMM algorithm with adaptive constraint

and penalty parameters to solve the CMS problem efficiently, to adapt to varying noise conditions, and also to enable automatic stopping of the algorithm once it has converged sufficiently.

- We show that in higher signal-to-noise ratio (SNR) regimes, our ADMM-CMS approach has less root mean squared error (RMSE) of localization and better successful recovery probability (SRP) compared to performing CS on each constituent sub-band.
- We also show that ADMM-CMS offers sharper spatial resolution and less noisy peaks, which translates to higher SRP, as compared to Bartlett-type BF. The results shown herein indicate the promise of ADMM-CMS as an efficient enabler of ISAC in FR3 for 6G systems.

Notations: \otimes denotes the Kronecker product and \odot denotes the element-wise product. Additionally, $\text{vec}(\cdot)$ denotes reshaping a matrix into a column vector, and $\text{vec}^{-1}(\cdot)$ denotes the inverse operation of $\text{vec}(\cdot)$. Also, \bar{a} denotes the complex conjugate of a , and $\{a_n\}_{n=1}^N$, which may also be written as $a_{1\dots N}$, denotes the set $\{a_1, a_2, \dots, a_N\}$. Moreover, $[a_n]_{n=1}^N$ is the vertically stacked vector $[a_1^T, a_2^T, \dots, a_N^T]^T$, and $\text{cat}_n\{\cdot\}$ denotes concatenating tensors along the n^{th} dimension. Finally, for some matrix \mathbf{A} , $[\mathbf{A}]_{i,:}$ denotes the i^{th} row of \mathbf{A} , $[\mathbf{A}]_{:,j}$ denotes the j^{th} column of \mathbf{A} , $[\mathbf{A}]_{i,j}$ denotes the $(i, j)^{\text{th}}$ element of \mathbf{A} , $\|\mathbf{A}\|_F$ denotes the Frobenius norm of \mathbf{A} , and $\|\mathbf{A}\|_{a,b}$ denotes the $\ell_{a,b}$ -mixed norm of \mathbf{A} .

II. SYSTEM MODEL

A. Multiband Channel and Signal Model

As shown in Fig. 1, we consider a reverse channel (e.g. uplink) scenario with one receiver (Rx) operating as a dual-function radar communication (DFRC) base station in bistatic mode on K sub-bands. There is one transmitting uplink communication user, and the channel consists of $N - 1$ scatterers. We consider both the user and the scatterers as *targets*, meaning that we are interested in localizing N targets. The Rx has M uniform linear array (ULA) antennas and operates on Q subcarriers per sub-band. We assume that the transmitter (Tx), Rx, and the scatterers are stationary, and the line-of-sight (LoS) signal is ideally always received. We need to know the angles of arrival (AoAs) and times of arrival (ToAs) to localize the targets. Because the Tx corresponds to the LoS path, the position of the Tx follows from the earliest ToA and the corresponding AoA. Once the Tx position is known, the remaining AoAs and the two-way ToAs are sufficient to determine the scatterer locations.

For the k^{th} sub-band, we consider the single-input, multiple-output (SIMO) channel in the frequency domain as follows.

$$\mathbf{H}_k = \sum_{n=1}^N g_{n,k} (\mathbf{a}_k^R(\theta_n)) (\mathbf{a}_k^F(\tau_n))^T \in \mathbb{C}^{M \times Q}, \quad (1)$$

where θ_n and τ_n are the AoA and the ToA of the n^{th} target, respectively, defined from the antenna broadside. The steering vectors are given by

$$\mathbf{a}_k^R(\theta) = [\exp(-j2\pi f_k(d_k/c)m \sin \theta)]_{m=0}^{M-1}, \quad (2)$$

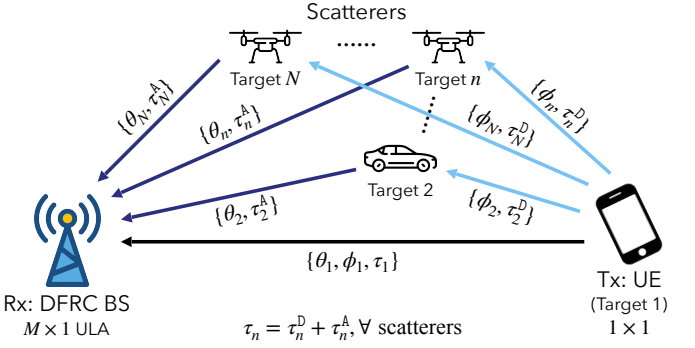


Fig. 1. The cellular ISAC scenario with one base station operating in bistatic mode and N targets, including one user device during uplink channel transmission and $N - 1$ scatterers within the range of the user device.

$$\mathbf{a}_k^F(\tau) = [\exp(-j2\pi(f_k + q\Delta f_k)\tau)]_{q=0}^{Q-1}, \quad (3)$$

where m is the Rx antenna index, q is the subcarrier index, f_k is the sub-band frequency, Δf_k is the subcarrier spacing, and d_k is the antenna spacing for the k^{th} sub-band. Note that we assume a simplified scenario where the antenna spacing differs per sub-band with $d_k = \lambda_k/2$, where $\lambda_k = c/f_k$ is the wavelength for sub-band k . The gain of the LoS path is modeled by the Friis' equation

$$g_{1,k} = \xi_{1,k} \sqrt{\frac{P^T \lambda_k^2 u^R(\theta_1) u^T(\phi_1)}{(4\pi)^2 (c\tau_1)^{\beta_k}}}, \quad (4)$$

and the gain of the n^{th} scatterer is modeled by the two-way bistatic radar equation

$$g_{n,k} = \xi_{n,k} \sqrt{\frac{P^T \lambda_k^2 u^R(\theta_n) u^T(\phi_n)}{(4\pi)^3 (c\tau_n^A)^{\beta_k} (c\tau_n^D)^{\beta_k}}}, \quad (5)$$

where P^T is the average transmit power, $u^T(\phi)$ and $u^R(\theta)$ are the antenna directivities, β_k is the distance pathloss exponent, $\xi_{n,k}$ is the complex path coefficient, ϕ_n is the angle of departure (AoD) defined from the antenna broadside, and τ_n^A and τ_n^D are the arrival and departure delays, respectively. Here, effects such as shadow fading can be absorbed into $\xi_{n,k}$.

Since the same stream of pilot symbols is received across antennas, we write the received signal at each sub-band as

$$\mathbf{Y}_k = \mathbf{H}_k \text{diag}(\mathbf{s}_k) + \mathbf{W}_k, \quad (6)$$

where $\mathbf{s}_k \in \mathbb{C}^{Q \times 1}$ are the transmitted QAM-modulated symbols across the subcarriers, and the noise follows $\text{vec}(\mathbf{W}_k) \sim \mathcal{CN}(\mathbf{0}, \sigma_k^2 \mathbf{I})$, where $\sigma_k^2 = \text{NF} \cdot N_0 \Delta f_k$, N_0 is the thermal noise power spectral density, and NF is the noise figure.

B. Problem Formulation

Note that \mathbf{Y}_k can be rewritten in vector form as

$$\text{vec}(\mathbf{Y}_k) = \sum_{n=1}^N g_{n,k} (\mathbf{s}_k \odot \mathbf{a}_k^F(\tau_n)) \otimes \mathbf{a}_k^R(\theta_n) + \text{vec}(\mathbf{W}_k). \quad (7)$$

We can think of the summation term due to the paths as a linear combination of the basis vectors

$$\mathcal{B}_k = \{\mathbf{s}_k \odot \mathbf{a}_k^F(\tau_n) \otimes \mathbf{a}_k^R(\theta_n)\}_{n=1}^N, \quad (8)$$

each corresponding to a ToA-AoA pair. In order to resolve the paths via CS, sparsity should be established in \mathcal{B}_k . We can do so by creating a “fat” dictionary matrix $\mathbf{A}_k = \mathbf{A}_k^F \otimes \mathbf{A}_k^R$ using very fine delay and angle grids to represent the basis vectors, which can be expressed by

$$\mathbf{A}_k^F = \text{cat}_2 \{ \mathbf{s}_k \odot \mathbf{a}_k^F(\tau) \}_{\tau \in \mathcal{T}} \in \mathbb{C}^{Q \times L^F}, \quad (9)$$

$$\mathbf{A}_k^R = \text{cat}_2 \{ \mathbf{a}_k^R(\theta) \}_{\theta \in \Theta} \in \mathbb{C}^{M \times L^R}, \quad (10)$$

and the grids are given by

$$\mathcal{T} = \{i\tau_{\max} / (L^F - 1) \mid i = 0, 1, \dots, L^F - 1\}, \quad (11)$$

$$\Theta = \{-\pi/2 + i\pi / (L^R - 1) \mid i = 0, 1, \dots, L^R - 1\}. \quad (12)$$

where L^F and L^R are the grid sizes of \mathcal{T} and Θ , respectively.

Now, we can express \mathbf{Y}_k in the following form:

$$\text{vec}(\mathbf{Y}_k) \approx \mathbf{A}_k \mathbf{x}_k + \text{vec}(\mathbf{W}_k), \quad (13)$$

where \mathbf{x}_k is the *sparse sensing vector* of the k^{th} sub-band, and the approximation error is due to the discretization error from using grid search. We can think of \mathbf{x}_k as activating some sparse columns in the fine matrix \mathbf{A}_k , each corresponding to a delay-angle pair closest to $\{\theta_n, \tau_n\}$. So, ideally, the value of each non-zero element of \mathbf{x}_k should approximate the corresponding $g_{n,k}$. We can further exploit the Kronecker structure to speed up computations by rewriting (13) in the following form

$$\mathbf{Y}_k = \mathbf{A}_k^R \text{vec}^{-1}(\mathbf{x}_k) \mathbf{A}_k^{F^T} + \mathbf{W}_k. \quad (14)$$

In order to localize the targets, we notice the following: as the ToAs and AoAs are expected to be similar across sub-bands, each \mathbf{x}_k should activate the same dictionary columns and hence have the same indices with non-zero elements. However, since the channel behavior varies across sub-bands, the values of those non-zero elements may vary. Thus, we want to enforce *structured sparsity*, which jointly optimizes for sparsity within each sub-band and preserves the same support *locations* across sub-bands. Ideally, we would need a constraint stating that each row of \mathbf{X} contains either all zeros or non-zero values. Nonetheless, since this constraint is very strict, we relax the problem for tractability by using certain norms as the minimization objective instead of using such constraints. To independently obtain the sparsest solution for each sub-band, an ℓ_1 -norm objective is typically proposed [16], so if we consider the multiband sparse sensing matrix $\mathbf{X} = \text{cat}_2 \{ \mathbf{x}_k \}_{k=1}^K$, one optimization objective to promote structured sparsity in \mathbf{X} is to minimize its $\ell_{2,1}$ -mixed norm, defined as

$$\|\mathbf{X}\|_{2,1} = \sum_{\ell=1}^{L^F L^R} \sqrt{\sum_{k=1}^K |\mathbf{X}_{\ell,k}|^2}. \quad (15)$$

We hence propose the following optimization problem for target localization:

$$(\mathcal{P}_{\text{CMS}}) : \begin{cases} \min_{\mathbf{X}} & \|\mathbf{X}\|_{2,1} \\ \text{s.t.} & \left\| \mathbf{Y}_k - \mathbf{A}_k^R \text{vec}^{-1}(\mathbf{x}_k) \mathbf{A}_k^{F^T} \right\|_F \leq \varepsilon_k, \forall k \end{cases} \quad (16)$$

where ε_k are the denoise thresholds.

III. ESTIMATION ALGORITHM

A. Target Localization

To solve the target localization problem posed in (16), we can use ADMM to decompose the solving process into simpler updates. First, we normalize \mathbf{Y}_k by $\tilde{\mathbf{Y}}_k = \mathbf{Y}_k / \|\mathbf{Y}_k\|_{F,2}$ to prevent signal power from impacting ε_k due to scaled reconstruction errors $\text{vec}(\mathbf{H}_k \text{diag}(\mathbf{s}_k)) - \mathbf{A}_k \mathbf{x}_k$ for different signal powers even at the same SNR. Then, following the structure in [17], we can introduce auxiliary variables $\mathbf{Z}_{1\dots K}$ and rewrite the problem in the form

$$(\mathcal{P}_{\text{ADMM}}) : \begin{cases} \min_{\mathbf{X}, \mathbf{Z}_{1\dots K}} & \|\mathbf{X}\|_{2,1} \\ \text{s.t.} & \mathbf{Z}_k \in \mathcal{C}_k, \\ & \mathbf{Z}_k = \mathbf{A}_k^R \text{vec}^{-1}(\mathbf{x}_k) \mathbf{A}_k^{F^T}, \forall k \end{cases} \quad (17)$$

where $\mathcal{C}_k = \left\{ \mathbf{Z}_k \mid \|\tilde{\mathbf{Y}}_k - \mathbf{Z}_k\|_F \leq \varepsilon_k \right\}$ is the convex feasible set of \mathbf{Z}_k . Hence, the augmented Lagrangian is given by

$$\begin{aligned} \mathcal{L}_\rho(\mathbf{X}, \mathbf{Z}_{1\dots K}, \mathbf{V}_{1\dots K}) = & \|\mathbf{X}\|_{2,1} + \sum_{k=1}^K \mathcal{I}_k(\mathbf{Z}_k) \\ & + \sum_{k=1}^K \text{tr}(\mathbf{U}_k^T (\mathbf{A}_k^R \text{vec}^{-1}(\mathbf{x}_k) \mathbf{A}_k^{F^T} - \mathbf{Z}_k)) \\ & + \sum_{k=1}^K \frac{\rho_k}{2} \left\| \mathbf{A}_k^R \text{vec}^{-1}(\mathbf{x}_k) \mathbf{A}_k^{F^T} - \mathbf{Z}_k \right\|_F^2, \end{aligned} \quad (18)$$

where ρ_k is the per-sub-band ADMM penalty factor, $\mathbf{V}_{1\dots K}$ contains the Lagrangian dual variables, and each feasible set \mathcal{C}_k can be enforced by this indicator function [17] [18]

$$\mathcal{I}_k(\mathbf{Z}_k) = \begin{cases} 0 & \text{if } \mathbf{Z}_k \in \mathcal{C}_k, \\ \infty & \text{otherwise.} \end{cases} \quad (19)$$

We then explain our variable update policies. First, we update \mathbf{X} while freezing $\mathbf{Z}_{1\dots K}$ and $\mathbf{V}_{1\dots K}$. From [17], in this step, we want to find \mathbf{X} that minimizes the augmented Lagrangian. The part of the augmented Lagrangian that we care about is only the first, third and fourth terms. Since the $\ell_{2,1}$ -mixed norm term is not smooth while the third and fourth terms are, we can use the proximal gradient descent method [18]. We start by computing the gradient for the smooth terms:

$$\begin{aligned} \nabla_{\mathbf{x}_k} \mathcal{L}_\rho = & \mathbf{A}_k^{R^H} \mathbf{V}_k \overline{\mathbf{A}_k^F} \\ & + \rho_k \mathbf{A}_k^{R^H} (\mathbf{A}_k^R \text{vec}^{-1}(\mathbf{x}_k) \mathbf{A}_k^{F^T} - \mathbf{Z}_k) \overline{\mathbf{A}_k^F}. \end{aligned} \quad (20)$$

To speed up computations, we can scale the dual variables. Let $\mathbf{U}_k = \mathbf{V}_k / \rho_k$, we can rewrite the gradient as

$$\nabla_{\mathbf{x}_k} \mathcal{L}_\rho = \rho_k \mathbf{A}_k^{R^H} (\mathbf{A}_k^R \text{vec}^{-1}(\mathbf{x}_k) \mathbf{A}_k^{F^T} - \mathbf{Z}_k + \mathbf{U}_k) \overline{\mathbf{A}_k^F}. \quad (21)$$

Denoting $\nabla_{\mathbf{X}} \mathcal{L}_\rho^{\text{smth}} = \text{cat}_2 \{ \nabla_{\mathbf{x}_k} \mathcal{L}_\rho^{\text{smth}} \}_{k=1}^K$, we update the target variable by applying a proximal operator of the objective function onto the smooth gradient descent result:

$$\mathbf{X}^{(i+1)} = \text{prox}_{\gamma \|\cdot\|_{2,1}} \left(\mathbf{X}^{(i)} - \gamma \nabla_{\mathbf{X}} \mathcal{L}_\rho^{\text{smth}} \right). \quad (22)$$

In our case, we use group soft thresholding, which is a common proximal operator for the $\ell_{2,1}$ -mixed norm:

$$\text{prox}_{\gamma \|\cdot\|_{2,1}}(\mathbf{C}) = \left[\max \left(0, 1 - \gamma / \|\mathbf{C}_{\ell,:}\|_2 \right) \mathbf{C}_{\ell,:} \right]_{\ell=1}^{N_C}, \quad (23)$$

where \mathbf{C} is some matrix with N_C rows. Since the $\nabla_{\mathbf{x}_k} \mathcal{L}'_\rho$ has the form $\rho_k (\mathbf{A}_k^H \mathbf{A}_k) \mathbf{x}_k + \mathbf{b}$, the step size is conservatively determined from the Lipschitz's constraint:

$$\gamma = \left(\max_k \left(\rho_k \|\mathbf{A}_k^F\|_2^2 \|\mathbf{A}_k^R\|_2^2 \right) \right)^{-1}. \quad (24)$$

Next we update $\mathbf{Z}_{1\dots K}$. From [17], in this step, we apply the proximal operator as follows:

$$\mathbf{Z}_k^{(i+1)} = \text{prox}_{\mathcal{I}_k(\cdot)} \left(\mathbf{A}_k^R \text{vec}^{-1} \left(\mathbf{x}_k^{(i+1)} \right) \mathbf{A}_k^{F^T} + \mathbf{U}_k^{(i)} \right), \forall k. \quad (25)$$

From [18], since we converted the inequality constraints using an indicator function, the proximal operator reduces to a Frobenius norm ball projection centered at $\tilde{\mathbf{Y}}_k$ with radius of ε_k :

$$\text{prox}_{\mathcal{I}_k(\cdot)}(\mathbf{C}) = \begin{cases} \mathbf{C} & \text{if } \mathbf{C} \in \mathcal{C}_k, \\ \tilde{\mathbf{Y}}_k + \varepsilon_k \cdot \frac{\mathbf{C} - \tilde{\mathbf{Y}}_k}{\|\mathbf{C} - \tilde{\mathbf{Y}}_k\|_F} & \text{otherwise.} \end{cases} \quad (26)$$

After that, we update $\mathbf{U}_{1\dots K}$ as described in [17]:

$$\mathbf{U}_k^{(i+1)} = \mathbf{U}_k^{(i)} + \mathbf{A}_k^R \text{vec}^{-1} \left(\mathbf{x}_k^{(i+1)} \right) \mathbf{A}_k^{F^T} - \mathbf{Z}_k^{(i+1)}, \forall k. \quad (27)$$

Finally, we combine the contributions from all sub-bands through arithmetic averaging. The output profile is given by

$$X(\theta, \tau) = \left[\frac{1}{K} \sum_{k=1}^K \text{vec}^{-1}(|\mathbf{x}_k^F|) \right]_{ij}, \forall \{\theta_i, \tau_j\} \in \Theta \times \mathcal{T}. \quad (28)$$

where \mathbf{x}_k^F is the final \mathbf{x}_k output. The support locations and the number of them are jointly estimated through performing peakfinding with a threshold on the normalized output profile:

$$\{\hat{\theta}_n, \hat{\tau}_n\} \in \arg \max_{\theta, \tau} \left(\max \left(r_{\text{pf}}, \frac{X(\theta, \tau)}{\max X(\theta, \tau)} \right) \right), \quad (29)$$

where r_{pf} is the peakfinding threshold. We denote the number of estimated peaks by \hat{N} .

B. Adaptive Learning Parameters

To maintain diversity between sub-bands and make the algorithm more efficient, we consider three aspects of adaptive learning parameters: adaptive ε_k , adaptive ρ_k , and automatic halt of the algorithm. We initialize ε_k by $\varepsilon_k^i = \alpha \|\tilde{\mathbf{Y}}_k\|_F$. Then, by observing the constraint residuals, we can loosen or tighten ε_k in the iterations through

$$\varepsilon_k^{(i+1)} = \varepsilon_k^{(i)} + \mu_\varepsilon \left(\left\| \tilde{\mathbf{Y}}_k - \mathbf{A}_k^R \text{vec}^{-1} \left(\mathbf{x}_k^{(i+1)} \right) \mathbf{A}_k^{F^T} \right\|_F - \varepsilon_k^{(i)} \right). \quad (30)$$

where ρ_k balances the primal and dual updates. Following the scheme from [17], in each iteration, we first calculate the per-sub-band primal residual

$$\text{p-res}_k^{(i+1)} = \left\| \mathbf{A}_k^R \text{vec}^{-1} \left(\mathbf{x}_k^{(i+1)} \right) \mathbf{A}_k^{F^T} - \mathbf{Z}_k^{(i+1)} \right\|_F \quad (31)$$

and the dual residual

$$\text{d-res}_k^{(i+1)} = \rho_k^{(i)} \left\| \mathbf{Z}_k^{(i+1)} - \mathbf{Z}_k^{(i)} \right\|_F. \quad (32)$$

We then update ρ_k in each iteration by

$$\rho_k^{(i+1)} = \begin{cases} \rho_k^{(i)} \mu_\rho & \text{if } \text{p-res}_k^{(i+1)} > r_\rho \text{d-res}_k^{(i+1)}, \\ \rho_k^{(i)} \mu_\rho^{-1} & \text{if } \text{d-res}_k^{(i+1)} > r_\rho \text{p-res}_k^{(i+1)}. \end{cases} \quad (33)$$

We finally rescale \mathbf{U}_k and recalculate γ after this step.

To decide when to halt ADMM automatically, we consider solution feasibility and stability by computing the primal and dual residuals [17]. In short, convergence is declared when

$$\begin{aligned} \text{p-res} &= \left\| [\text{p-res}_k]_{k=1}^K \right\|_2 \leq \epsilon_{\text{prim}}, \\ \text{d-res} &= \left\| [\text{d-res}_k]_{k=1}^K \right\|_2 \leq \epsilon_{\text{dual}}, \end{aligned} \quad (34)$$

where ϵ_{prim} and ϵ_{dual} are the primal and dual tolerances, respectively. Similar to the residuals, we first calculate the per-sub-band tolerances as outlined in [17] using specified absolute and relative tolerances ϵ_{abs} and ϵ_{rel} , respectively, and then aggregate across sub-bands using the ℓ_2 -norm approach. A summary of the entire ADMM-CMS algorithm is given in Algorithm 1.

IV. SIMULATION RESULTS

A. Comparison Benchmark

A Bartlett-type BF-based approach is used in [10]. To adapt this benchmark to multiband sensing, we calculate the output

Algorithm 1: ADMM-CMS

```

Input:  $\{\mathbf{Y}_k, \mathbf{s}_k\}_{k=1}^K$ 
Output:  $\{\hat{\theta}_n, \hat{\tau}_n\}_{n=1}^{\hat{N}}, \hat{N}$ 
 $\tilde{\mathbf{Y}}_k \leftarrow \mathbf{Y}_k / \|\mathbf{Y}_k\|_{F,2}, \forall k$ 
Compute  $\mathbf{A}_k^R, \forall k$  by (10)
Compute  $\mathbf{A}_k^F, \forall k$  by (9)
Initialize  $\{\mathbf{X}, \mathbf{Z}_k, \mathbf{U}_k\} \leftarrow 0, \varepsilon_k \leftarrow \varepsilon_k^i, \rho_k \leftarrow \rho^i, \forall k$ 
Initialize  $\gamma$  by (24)
for  $i = 1$  to  $\text{max\_iter}$  do
  Compute  $\nabla_{\mathbf{x}_k} \mathcal{L}_\rho^{\text{smth}}, \forall k$  by (21)
   $\nabla_{\mathbf{X}} \mathcal{L}_\rho^{\text{smth}} \leftarrow \text{cat}_2 \left\{ \nabla_{\mathbf{x}_k} \mathcal{L}_\rho^{\text{smth}} \right\}_{k=1}^K$ 
  Update  $\mathbf{X}$  by (22) (23)
  for  $k = 1$  to  $K$  do
    Update  $\mathbf{Z}_k$  by (25) (26)
    Update  $\mathbf{U}_k$  by (27)
    Update p-res $_k$  by (31)
    Update d-res $_k$  by (32)
    Update  $\rho_k$  by (33)
     $\mathbf{U}_k \leftarrow \mathbf{U}_k / \mu_\rho$  or  $\mathbf{U}_k / \mu_\rho^{-1}$  depending on (33)
    Update  $\varepsilon_k$  by (30)
  Compute  $\gamma$  by (24)
  Compute  $\epsilon_{\text{prim}}$  and  $\epsilon_{\text{dual}}$  as outlined in [17]
  if (34) then
    break
Estimate  $\{\hat{\theta}_n, \hat{\tau}_n\}, \forall n$  and  $\hat{N}$  by (28) (29)

```

TABLE I
SIMULATION PARAMETERS

System Parameters			
N	2	M	60
Q	100	K	2
f_k	{7, 10} GHz (FR3)	Δf_k	{1800, 3000} kHz
β_k	1.34, $\forall k$ [5]	Modulation	4-QAM
d_k	$\lambda_k/2$	P^T	-70 to -20 dBm
N_0	-174 dBm/Hz	NF	7 dB
τ_{\max}	200 ns	$\xi_{n,k}$	{1, 5}, $\forall k$ (Fig. 3); 1, $\forall n, k$ (Fig. 4)
Sensing Parameters			
τ_n	{40.03, 45.08} ns	θ_n	{0, 45.2}°
Algorithm Parameters			
max_iter	10^4	num_MC	900
L^F	201 (1 ns steps)	L^R	181 (1° steps)
α	0.01	μ_ε	0.3
ρ^1	0.2	μ_ρ	1.001
r_ρ	10	r_{pf}	0.2 (Fig. 3); 0.02 (Fig. 4)
ϵ_{abs}	10^{-8}	ϵ_{rel}	10^{-5}

power profile for all $\{\theta_i, \tau_j\} \in \Theta \times \mathcal{T}$ by

$$P(\theta, \tau) = \frac{1}{K} \sum_{k=1}^K \left| (\mathbf{s}_k \odot \mathbf{a}_k^F(\tau_j))^T \mathbf{Y}_k^H (\mathbf{a}_k^R(\theta_i)) \right|, \quad (35)$$

and then perform a peakfinding similar to (29) for $P(\theta, \tau)$.

B. Metrics

One of the metrics used is the RMSE, where we only consider errors of the true and estimated points pairs that are optimally matched without replacement using the Hungarian algorithm. This is because we are doing joint estimation and detection, so the number of estimated targets may be different from the actual number of targets. We evaluate the RMSE for both AoAs and ToAs.

Another metric that we consider is the SRP, which focuses only on localization performance. It is defined as the fraction of all Monte Carlo simulations that has $\hat{N} = N$, $|\hat{\theta}_n - \theta_n| \leq 1^\circ, \forall n$, and $|\hat{\tau}_n - \tau_n| \leq 1 \text{ ns}, \forall n$ satisfied simultaneously.

C. Simulation Implementation

For simplicity, we assume omnidirectional antennas, hence $u^T(\phi) = u^R(\theta) = 1$. A table of all parameters is provided in Table I, where num_MC is the number of Monte Carlo iterations. Note that in the proposed numerology of FR3, we expect higher bandwidths at higher sub-bands [8]. We predefine the Tx, Rx, and target locations by geometry. Next, we convert the Cartesian coordinates to AoAs, AoDs, and ToAs. These sensing parameters are intentionally generated off-grid for better visualization of the RMSE. The test variable is P^T .

D. Results and Discussion

From Fig. 2, it is obvious that under the same system parameters, our ADMM-CMS produces much sharper and

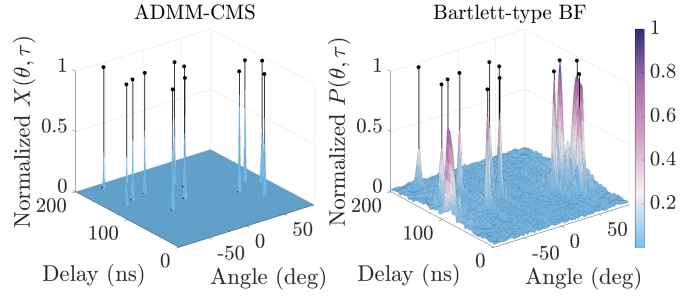


Fig. 2. Sample normalized $X(\theta, \tau)$ of our ADMM-CMS and $P(\theta, \tau)$ of the Bartlett-type BF benchmark. The black lines correspond to the true AoAs and ToAs, and $P^T = -25$ dBm.

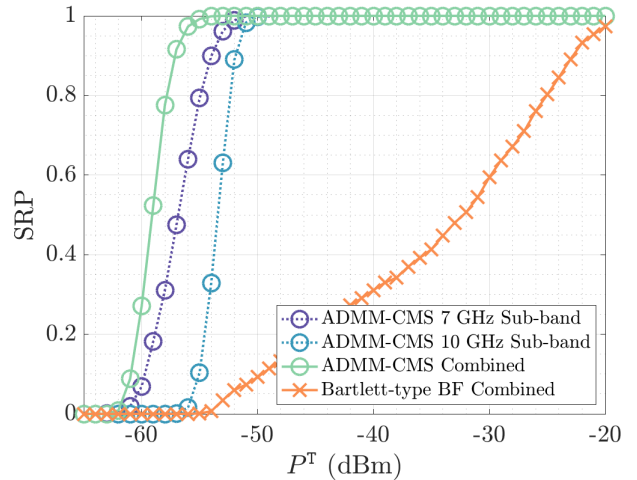


Fig. 3. SRP vs. P^T for one LoS path and one scatterer for both ADMM-CMS and the Bartlett-type BF benchmark. The number of Monte Carlo iterations is 900.

less noisy peaks compared to the Bartlett-type BF benchmark, which implies improved detection and resolution.

As a result, from Fig. 3, it can be observed that compared to the benchmark, our ADMM-CMS achieves significantly better SRP performance especially in the high SNR region (at $P^T = -62$ dBm and above). For example, for an SRP of 0.9, the ADMM-CMS requires only about -57 dBm as opposed to -23 dBm for the Bartlett-type BF benchmark. One contributor to this large gain is that even at high SNR, the $P(\theta, \tau)$ profile for the Bartlett-type BF benchmark contains sinc-shaped artifacts along the axes corresponding to the estimated ToAs and AoAs. Moreover, we can also see significant SRP gains of ADMM-CMS compared to performing CS on the constituent sub-bands. For instance, at the same SNR of $P^T = -56$ dBm, the combined case has an SRP of 0.97, while those for lower and higher sub-bands are only 0.65 and 0.02, respectively.

From Fig. 4, we can see that the ADMM-CMS also achieves a better RMSE than performing CS on the constituent sub-bands in the high SNR region (at $P^T = -46$ dBm and above). For instance, at -41 dBm, the combined case has a delay RMSE of about 0.13 ns while those for lower and higher sub-bands are around 0.20 and 0.21 ns, respectively. However, in the RMSE figure, we can see that the start of the high SNR

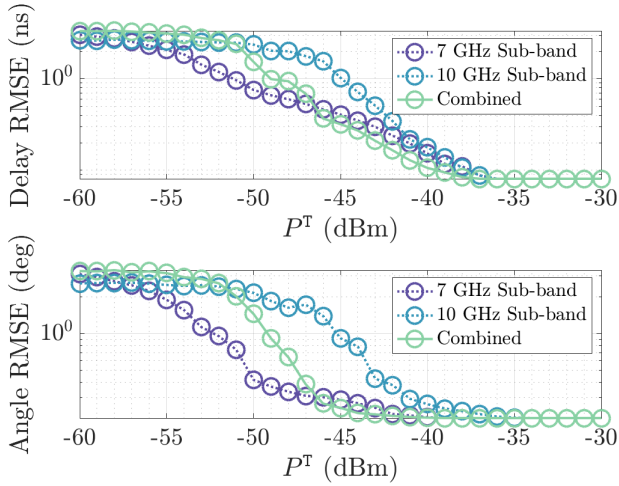


Fig. 4. Delay and angle RMSE vs. P^T for one LoS path and one scatterer for ADMM-CMS. The number of Monte Carlo iterations is 900.

region (signaled by the end of the waterfall region) for the combined case lies between that of the constituent sub-bands, while in the SRP figure, the combined case shows an earlier start of the transition region compared to the sub-bands.

V. CONCLUSION AND FUTURE WORK

This paper has shown that with the same 100 received pilot symbols across 60 antennas, the proposed ADMM-CMS method achieves substantially better performance than the benchmark approaches. First, ADMM-CMS produces sharper delay-angle resolution and stronger denoising than Bartlett BF, leading to higher SRP. For example, to attain an SRP of 0.9, ADMM-CMS achieves a 34 dB gain in P^T as compared to Barlett BF, which demonstrates that enforcing structured sparsity across sub-bands effectively suppresses noise and false artifacts, improving target detection. Second, ADMM-CMS outperforms compressed sensing applied independently to constituent sub-bands using the same ADMM framework in terms of estimation accuracy and target detection. For instance, under $P^T = -41$ dBm, ADMM-CMS reduces the delay RMSE by 35% and 38.1%, respectively, compared to separately employing the constituent 7 and 10 GHz sub-bands, which shows that leveraging multiple sub-bands greatly enhances localization accuracy.

Together, these findings establish ADMM-CMS as a practical enabler of ISAC in FR3, offering both target detectability and spacial resolution advantages critical for future 6G applications such as the internet of things, smart cities, and autonomous driving. For future work, a more realistic channel model with sub-band frequency dependent dense multipath components [19], [20] and identical antenna spacing across all sub-bands can be explored.

ACKNOWLEDGMENTS

This work is supported by Tamkeen under the Research Institute NYUAD grant CG017, and the New York University (NYU) WIRELESS Industrial Affiliates Program.

REFERENCES

- [1] M. Chafii, L. Bariah, S. Muhandat, and M. Debbah, "Twelve Scientific Challenges for 6G: Rethinking the Foundations of Communications Theory," *IEEE Communications Surveys & Tutorials*, pp. 1–1, 2023.
- [2] T. S. Rappaport, Y. Xing, O. Kanhere, S. Ju, A. Madanayake, S. Mandal, A. Alkateeb, and G. C. Trichopoulos, "Wireless Communications and Applications Above 100 GHz: Opportunities and Challenges for 6G and Beyond," *IEEE Access*, vol. 7, pp. 78 729–78 757, 2019.
- [3] D. Wu, W.-P. Zhu, and M. Swamy, "A Compressive Sensing Method for Noise Reduction of Speech and Audio Signals," in *2011 IEEE 54th International Midwest Symposium on Circuits and Systems (MWSCAS)*, 2011, pp. 1–4.
- [4] D. Shakya *et al.*, "Urban Outdoor Propagation Measurements and Channel Models at 6.75 GHz FR1(C) and 16.95 GHz FR3 Upper Mid-Band Spectrum for 5G and 6G," in *IEEE ICC 2025*, 2025, pp. 1–6.
- [5] D. Shakya, M. Ying, T. S. Rappaport, H. Poddar, P. Ma, Y. Wang, and I. Al-Wazani, "Comprehensive FR1(C) and FR3 Lower and Upper Mid-Band Propagation and Material Penetration Loss Measurements and Channel Models in Indoor Environment for 5G and 6G," *IEEE Open Journal of the Communications Society*, vol. 5, pp. 5192–5218, 2024.
- [6] M. Ying, D. Shakya, T. S. Rappaport, P. Ma, Y. Wang, I. Al-Wazani, Y. Wu, and H. Poddar, "Upper Mid-Band Channel Measurements and Characterization at 6.75 GHz FR1(C) and 16.95 GHz FR3 in an Indoor Factory Scenario," in *IEEE ICC 2025*, 2025, pp. 1–6.
- [7] D. Shakya *et al.*, "Wideband Penetration Loss through Building Materials and Partitions at 6.75 GHz in FR1(C) and 16.95 GHz in the FR3 Upper Mid-band spectrum," in *IEEE GLOBECOM 2024*, 2024, pp. 1–6.
- [8] A. Bazzi, R. Bomfin, M. Mezzavilla, S. Rangan, T. S. Rappaport, and M. Chafii, "Upper Mid-Band Spectrum for 6G: Vision, Opportunity and Challenges," accepted in *IEEE Communications Magazine*, 2025.
- [9] T. S. Rappaport, D. Shakya, and M. Ying, "Point data for site-specific mid-band radio propagation channel statistics in the indoor hotspot (InH) environment for 3GPP and Next Generation Alliance (NGA) channel modeling," in *IEEE International Communications Conference (ICC) 2025*, 2025, pp. 1–6.
- [10] T. Raviv, S. Kang, M. Mezzavilla, S. Rangan, and N. Shlezinger, "Multi-Frequency Upper Mid-Band Localization," in *2024 IEEE 25th International Workshop on Signal Processing Advances in Wireless Communications (SPAWC)*, 2024, pp. 736–740.
- [11] M.-Y. Gong and B. Lyu, "EM and SAGE Algorithms for DOA Estimation in the Presence of Unknown Uniform Noise," *Sensors*, vol. 23, no. 10, p. 4811, 2023.
- [12] J. C. Liberti and T. S. Rappaport, *Smart antennas for wireless communications: IS-95 and third generation CDMA applications*. Prentice Hall PTR, 1999.
- [13] X. Wang, F. Zhu, C. Huang, A. Alhammadi, F. Bader, Z. Zhang, C. Yuen, and M. Debbah, "Robust Beamforming With Gradient-Based Liquid Neural Network," *IEEE Wireless Communications Letters*, vol. 13, no. 11, pp. 3020–3024, 2024.
- [14] Y. Chi and Y. Chen, "Compressive two-dimensional harmonic retrieval via atomic norm minimization," *IEEE Transactions on Signal Processing*, vol. 63, no. 4, pp. 1030–1042, 2015.
- [15] A. Liu, X. Liu, Y. Zeng, and V. K. N. Lau, "Cramér–Rao bounds for joint delay and angle estimation in compressive sensing radar," *IEEE Transactions on Signal Processing*, vol. 66, no. 18, pp. 4772–4787, 2018.
- [16] D. L. Donoho, "For most large underdetermined systems of linear equations the minimal ℓ_1 -norm solution is also the sparsest solution," *Communications on Pure and Applied Mathematics: A Journal Issued by the Courant Institute of Mathematical Sciences*, vol. 59, no. 6, pp. 797–829, 2006.
- [17] S. Boyd, N. Parikh, E. Chu, B. Peleato, J. Eckstein *et al.*, "Distributed optimization and statistical learning via the alternating direction method of multipliers," *Foundations and Trends® in Machine learning*, vol. 3, no. 1, pp. 1–122, 2011.
- [18] N. Parikh, S. Boyd *et al.*, "Proximal algorithms," *Foundations and trends® in Optimization*, vol. 1, no. 3, pp. 127–239, 2014.
- [19] S. Jiang, W. Wang, Y. Miao, W. Fan, and A. F. Molisch, "A Survey of Dense Multipath and Its Impact on Wireless Systems," *IEEE Open Journal of Antennas and Propagation*, vol. 3, pp. 435–460, 2022.
- [20] M. Ying, D. Shakya, P. Ma, G. Qian, and T. S. Rappaport, "Site-Specific Location Calibration and Validation of Ray-Tracing Simulator NYURay at Upper Mid-Band Frequencies," submitted to *npj Wireless Technology*, Jul. 2025.